THE JOURNAL OF PHYSICAL CHEMISTRY C
A JOURNAL OF THE AMERICAN CHEMICAL SOCIETY

pubs.acs.org/JPCC

Article

Superconductivity in Bismuth Pyrochlore Lattice Compounds $RbBi_2$ and $CsBi_2$: The Role of Relativistic Effects

Sylwia Gutowska, Bartlomiej Wiendlocha, Tomasz Klimczuk, and Michał J. Winiarski*

Cite This: *J. Phys. Chem. C* 2023, 127, 14402−14414

Read Online

ACCESS | Metrics & More | Article Recommendations | Supporting Information

ABSTRACT: Superconducting properties of two bismuthide intermetallic compounds, $RbBi_2$ and $CsBi_2$, were studied by means of experimental measurements and *ab initio* calculations. We show that in both compounds, the superconductivity emerges from the pyrochlore Bi lattice and its formation is heavily influenced by relativistic effects. Based on our analysis of the effect of spin−orbit coupling on the electron−phonon coupling, we suggest a possible criterion for finding new superconducting materials by looking for structures featuring relativistically stabilized hypervalent networks of heavy *p*-block elements.

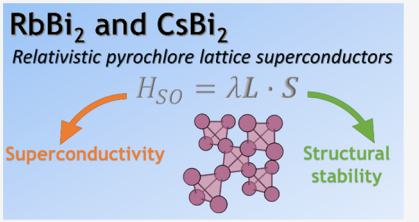

Downloaded via GDANSK UNIVERSITY OF TECHNOLOGY on July 31, 2023 at 10:55:03 (UTC).
See https://pubs.acs.org/sharingguidelines for options on how to legitimately share published articles.

INTRODUCTION

Bismuth ($Z = 83$) is the heaviest stable element of the periodic table (the half-life of the longest living isotope, ^{209}Bi $\tau_{1/2} = 2.0 \times 10^{19}$ yr[1] is 9 orders of magnitude longer than the age of the universe, $t = 1.4 \times 10^{10}$ yr). This property makes it and its compounds interesting for studying effects of strong spin−orbit coupling (SOC) on physical properties of materials. Relativistic effects often result in Bi compounds behaving differently than isoelectronic species. For example, the most common cationic oxidation state of Bi is +3, with +5 compounds being generally unstable toward reduction.[2−4] Bi^{3+} cation is very often lone-pair active, leading to complicated coordination environments.[1] Less known are the effects of relativistic phenomena on structural chemistry of Bi intermetallic compounds. Bi is known to form several stable hypervalent polyanions, such as the Bi^- square network found in LiBi and NaBi but not observed in the isoelectronic NaSb.[5−8] Similarly, $CaBi_2$ and the recently reported $SrBi_2$ both host a hypervalent Bi^- square lattice,[9,10] which is missing in the isoelectronic $CaSb_2$.[11]

A number of binary bismuth superconductors are known, including the following: $Ca_{11}Bi_{10-x}$,[12] $CaBi_2$,[13,14] $SrBi_3$,[15,16] $BaBi_3$,[17] Ba_2Bi_3,[18] LiBi,[8,19] NaBi,[7] KBi_2 $RbBi_2$, and $CsBi_2$.[20] The latter three compounds are cubic Laves phases, crystallizing in a relatively simple $MgCu_2$-type structure in which Bi atoms form a pyrochlore (vertex sharing tetrahedral) network (Figure 1). Interestingly, while the $MgCu_2$ is the 5th most common binary intermetallic structure type,[21] only a few of the known compounds feature a *p*-block element occupying the pyrochlore network—besides the three dibismuthides, these are $MgIn_2$,[22] SnS_2,[23] and RAl_2 (R = Sr, Ba, rare-earth metals, Th, and U).

Here, we present the results of our experimental and computational studies on $RbBi_2$ and $CsBi_2$, concentrated on the effects of strong SOC on superconducting properties. We describe the magnetic behavior of single-crystalline samples of the two compounds, showing that type-I superconductivity is observed in both compounds. Heat capacity measurements show moderate to strong electron−phonon coupling. Based on the results of electronic and phonon structure calculations, we show that in both compounds, superconductivity emerges from the Bi_4^{2-} pyrochlore lattice and that the relativistic effects play a complex role in stability and properties of the two phases. We found that strong SOC is crucial for the stability of charged Bi pyrochlore network and discuss the implications of this fact for the search for new heavy element-bearing superconducting materials.

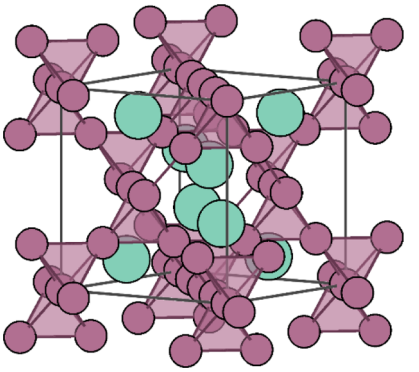

Figure 1. Crystal structure of the cubic Laves phases ABi_2 (A = K, Rb, Cs). Bi atoms (drawn in purple) form a vertex-sharing tetrahedral (pyrochlore) lattice with voids filled with alkali atoms (green).

Received: March 31, 2023
Revised: May 18, 2023
Published: July 13, 2023

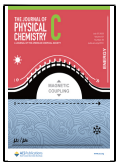

ACS Publications

© 2023 The Authors. Published by American Chemical Society

MATERIALS AND METHODS

Single crystals of $RbBi_2$ and $CsBi_2$ were grown using a Bi self-flux method. Pieces of bismuth (Alfa Aesar, 99.99%) and rubidium (Alfa Aesar, 99.9%) were put in an alumina crucible inside an Ar-filled glovebox. Cesium was first heated above its melting point by warming it in hand and then poured dropwise into the crucible and covered with Bi pieces. Crucibles were then put in fused silica tubes along with plugs of quartz wool, and the tubes were subsequently evacuated, back-filled with Ar, and sealed without exposing alkaline metals to air. They were then heated to 550 °C, kept at that temperature for 8 h, and then slowly cooled (5 °C per h) to 310 °C at which temperature the excess Bi was spun off with the aid of a centrifuge. Clusters of tetrahedrally shaped crystals were obtained, with sizes ranging up to ca. 1 mm.

Warning! Rubidium and cesium metals will ignite spontaneously when exposed to air. Special care needs to be taken to avoid fire. ABi_2 single crystals will decompose in air within minutes and the reaction might be exothermic.

The phase identity of the crystals was examined using powder X-ray diffraction (PXRD) measurements employing a Bruker D8 FOCUS diffractometer with a Cu Kα radiation source and a LynxEye detector. A few single crystals were crushed for the PXRD measurements inside an Ar-filled glovebox and mixed with an Apiezon-N grease or petroleum jelly. Since the powdered samples quickly oxidize, reacting with oxygen and moisture from air, the scanning time had to be reduced to 8 min. PXRD patterns were then analyzed by means of the LeBail method[24] using the FullProf software package.[25] PXRD patterns taken after a prolonged exposition to air show that both compounds decomposed completely yielding weakly crystalline elemental Bi and an amorphous product (most probably a hydrated alkali metal hydroxide), similarly to what was observed in $CaBi_2$.[13]

Heat capacity measurements were performed using the Quantum Design PPMS system by the standard relaxation technique. Magnetic susceptibility measurements were carried out using the ACMS option of the PPMS. Multiple randomly oriented single crystals were put in the standard straw sample holders. Sample preparation was carried out inside a glovebox to prevent oxidation.

Ab initio calculations were performed using the Quantum Espresso (QE) package[26] employing ultrasoft Perdew–Burke–Ernzerhof (PBE) GGA[27] pseudopotentials[28] with valence configuration $4s^25s^14p^6$ for rubidium, $5s^26s^15p^6$ for cesium and $6s^26p^35d^{10}$ for bismuth, whereas wave function and charge density energy cutoffs were set to values 50 Ry and 500 Ry, respectively. For the consideration of the influence of the relativistic effects, two types of calculations were performed: scalar-relativistic (neglecting SOC) and fully relativistic (with SOC effect included for Bi). As expected and tested, inclusion of SOC for Rb and Cs does not change the results of calculations; thus, the SOC was included only for Bi in final calculations. In the first step, the lattice constant was optimized using the Broyden–Fletcher–Shanno–Goldfarb (BFGS) method. The electronic structure was calculated at the grid of $(24)^3$ *k*-points. Phonon structure and properties of electron–phonon coupling (EPC) were calculated at a grid of $(6)^3$ *q*-points.

Chemical bonding was investigated by means of Crystal Orbital Hamilton Population analysis[29,30] using the Stuttgart TB-LMTO-ASA code.[31,32] Calculations were performed using the experimental cell parameter and $(32)^3$ *k*-point mesh and employed the Perdew–Wang GGA[33] exchange–correlation (*xc*) potential.

Electronic structure of an isolated tetrahedral Bi_4 cluster was calculated using the ReSpect 5.1.0 relativistic DFT code.[34] Scalar-relativistic calculations were performed by means of 1-component Kohn–Sham method with one-electron relativistic corrections due to Douglas–Kroll–Hess of the second order (1c KS-DKH2). Fully relativistic electronic structure was calculated using the four-component Dirac-Kohn-Sham Hamiltonian (4c DKS). The Dyall core–valence double-zeta basis set[35] and the PBE xc potential were used in both cases. Molecular orbitals obtained from the 1c KS-DKH2 calculations were visualized using the IboView program.[36,37]

RESULTS AND DISCUSSION

Room-temperature PXRD patterns of crushed crystals are presented in Figure S1 of the Supporting Information. All the Bragg lines in the PXRD pattern can be indexed to cubic (space group $Fd\bar{3}m$, #227) unit cell of ABi_2 and elemental Bi (both from leftover flux droplets and decomposition of material). Lattice parameters resulting from LeBail fits are in agreement with previous reports.[38,39] Details of crystal structures are gathered in Table S1 of the Supporting Information.

The Rb–Rb and Cs–Cs distances are 4.20 and 4.26 Å, significantly shorter than in their elemental form (4.89 and 5.29 Å, respectively[40,41]), while Bi–Bi spacing is larger than in elemental Bi (3.47 vs 3.07 Å[42]) and in the Bi_4 cluster (2.98 Å as obtained by *ab initio* structural relaxation). This highlights the electron transfer from the electropositive alkali metal to the Bi network.

To characterize superconducting transitions of ABi_2, *dc* magnetization was measured in the temperature interval T = 1.9–5 K. The plot of low-field (H_{dc} = 20 Oe) volume susceptibility (χ_V) versus temperature is shown in Figure 2a,b). Sharp transition to a full Meissner state (χ_V reaching the value

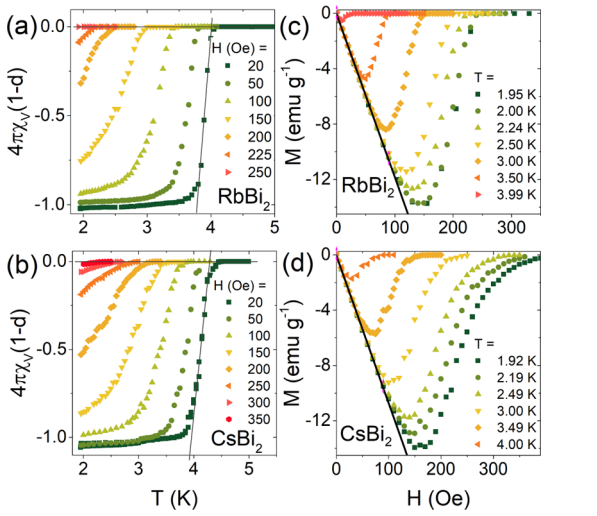

Figure 2. (a,b) Temperature-dependent magnetic susceptibility of $RbBi_2$ and $CsBi_2$. A sharp transition to the Meissner state is seen at the T_c. Susceptibility data were corrected for the demagnetization factor (see the text). (c,d) Field-dependent magnetization curves showing a typical type-I character of superconductivity for $RbBi_2$ and an ambiguous type-I/type-II behavior for $CsBi_2$.

MOST WIEDZY Downloaded from mostwiedzy.pl

https://doi.org/10.1021/acs.jpcc.3c02176
J. Phys. Chem. C 2023, 127, 14402–14414

of -4π after correcting for the demagnetization effect) was observed in both materials. Very small difference between zero-field cooled and field-cooled (FC) magnetization (not shown) is indicative of high crystal quality.

Field-dependent magnetization below the critical temperature is shown in Figure 2c,d. In the case of $RbBi_2$, the shape of the magnetization curve is consistent with a type-I superconducting transition with an influence of the demagnetization effect due to randomly oriented crystalline grains.[13,43] In $CsBi_2$, the shape of the M versus H curve has a tail-like feature at higher fields, which is more consistent with type-II SC; however, the low critical field suggests type-I behavior. Assuming a perfect diamagnetic linear response to the magnetic field, the M_v versus H data at the lowest temperature (T = 1.92 K and T = 1.95 K for Rb- and Cs-bearing compound, respectively) were fitted with a linear function ($M_{fit} = aH + b$). The value of the demagnetization factor (d) is calculated using the equation $-a = (4\pi(1 - d))^{-1}$, yielding d = 0.676 for $RbBi_2$ and d = 0.744 for $CsBi_2$.

The fields at which deviations from a linear response occur were taken as thermodynamic critical fields H_c*. The H_c* values derived for different temperatures are fitted with the equation $H_c^*(T) = H_c^*(0)[1 - (T/T_c)^2]$.[44] The values of critical field extrapolated to T = 0 K using the fitted function are $H_c^*(0)$ = 127 Oe for $RbBi_2$ and $H_c^*(0)$ = 146 Oe for $CsBi_2$ (see Figure S2 of the Supporting Information). This value has to be corrected for the demagnetization factor, yielding $H_c(0)$ = 188 Oe and 196 Oe, respectively.

The heat capacity measured through the superconducting transition in ABi_2 is shown in Figure 3. Bulk nature of the superconductivity is confirmed by large, sharp anomalies at T_c = 4.24 K and 4.65 K for $RbBi_2$ and $CsBi_2$, respectively. It is worth noting that under applied field, the jump at T_c becomes larger than at zero field in both compounds. A similar effect was observed, e.g., in KBi_2,[45] $ScGa_3$, $LuGa_3$,[46] $YbSb_2$,[47] $ReAl_6$,[48] and $LiPd_2Ge$[49] type-I superconductors. This suggests that both $RbBi_2$ and $CsBi_2$ can be classified as type-I superconductors. It is worth noting that type-I superconductivity, especially with T_c > 2 K, is rather uncommon among intermetallic compounds.

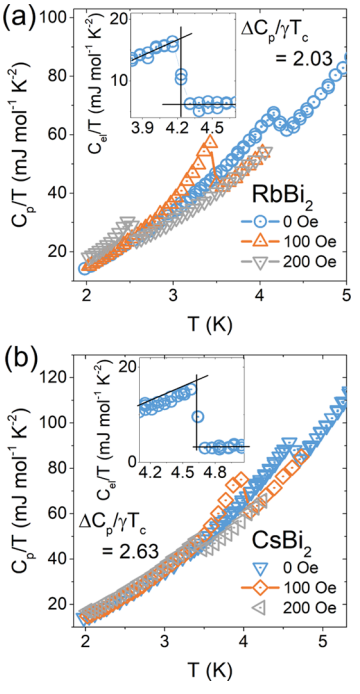

Figure 3. Low-temperature heat capacity of (a) $RbBi_2$ and (b) $CsBi_2$, showing an anomaly at the superconducting critical temperature (enlarged in insets). The normalized heat capacity jump $\Delta C_p/\gamma T_c$ is calculated using γ values estimated from a fit presented in Figure S2 of the Supporting Information. Note that in both cases, the jump under an applied magnetic field is found to be larger than at zero field, which is a typical behavior for type-I superconductors (see, e.g., refs 45−49).

Figure S3 of the Supporting Information presents the low-temperature C_p/T versus T^2 plots for both materials. Electronic (γ) and vibrational (β) heat capacity contributions were extracted by fitting the data with relation $C_p/T = \gamma + \beta T^2$. The fit yields very similar γ values (5.0 and 4.9 mJ mol^{-1} K^{-2}) for both materials. The normalized heat capacity jumps at T_c estimated by using the equal entropy construction method (see insets of Figure 5a,b), are $\Delta C_p/\gamma T_c$ = 2.03 for $RbBi_2$ and $\Delta C_p/\gamma T_c$ = 2.63 for $CsBi_2$, both well above the BCS limit for a weakly coupled superconductor (1.43).

The Debye temperature (Θ_D) is calculated from the β specific heat coefficients using the relation

$$\Theta_D = \sqrt[3]{\frac{12\pi^4 nR}{5\beta}}$$

This yields Θ_D = 127(1) for $RbBi_2$ and 123(1) K for $CsBi_2$, both values being slightly higher than for elemental Bi (Θ_D = 112 K). Taking Θ_D and T_c values and assuming the value of the Coulomb pseudopotential parameter μ^* = 0.13, the electron−phonon coupling parameter (λ_{el-ph}) can be estimated using the modified McMillan formula

$$\lambda = \frac{1.04 + \mu^* \ln\left(\frac{\Theta_D}{1.45T_c}\right)}{(1 - 0.62\mu^*)\ln\left(\frac{\Theta_D}{1.45T_c}\right) - 1.04}$$

For $RbBi_2$, this gives λ = 0.82 and for $CsBi_2$ λ = 0.87, both values being indicative of moderate coupling strength.

Table 1 summarizes the normal and superconducting state parameters derived from experimental measurements.

In order to gain insight into the role played by relativistic effects in the formation of superconducting state in the two compounds, we analyzed their electronic and phonon structure by means of *ab initio* calculations.

Charge transfer from the Rb/Cs to Bi is evident from the electronic density of $RbBi_2$ and $CsBi_2$ (Figure 4), and the Bader charge analysis yields $Rb^{+0.71}(Bi_2)^{-0.71}$ and $Cs^{+0.64}(Bi_2)^{-0.64}$. This is consistent with electronegativity difference (0.82/0.79 vs 2.02 for Rb/Cs and Bi in the Mulliken scale, respectively) and the observed shortening of Bi−Bi bonds with respect to the elemental Bi. The density distribution along the Bi−Bi bonds has a strongly delocalized, metallic character. Since charge density is concentrated on the Bi framework, both compounds can be viewed as pyrochlore metals. As we will further show, the electron−phonon coupling resulting in superconductivity in ABi_2 (A = Rb, Cs) also stems from the Bi pyrochlore sublattice.

The electronic band structure and electronic density of states (DOS) for both compounds are shown in Figure 5. The band structure around the Fermi level is similar in both cases. The Fermi level lies within a peak of DOS; thus, even a small difference of band structure detailed below, lead to higher DOS at Fermi level in the case of $CsBi_2$ (DOS(E_F) = 1.51

https://doi.org/10.1021/acs.jpcc.3c02176
J. Phys. Chem. C 2023, 127, 14402−14414

MOST WIEDZY Downloaded from mostwiedzy.pl

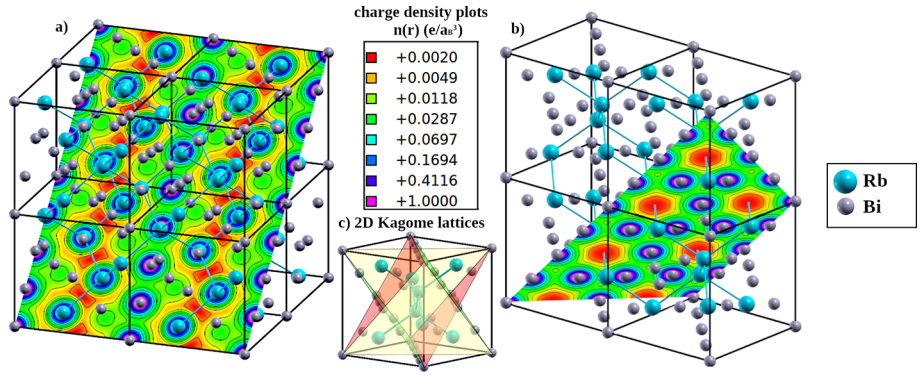

Figure 4. Charge density of supercell of $RbBi_2$ plotted in the (110) plane (a) and (111) plane (b); the charge density in (111) plane is similar to 2D kagom lattice marked; however, there are many of such planes in the unit cell (c) resulting in 3D character of electronic bonds.

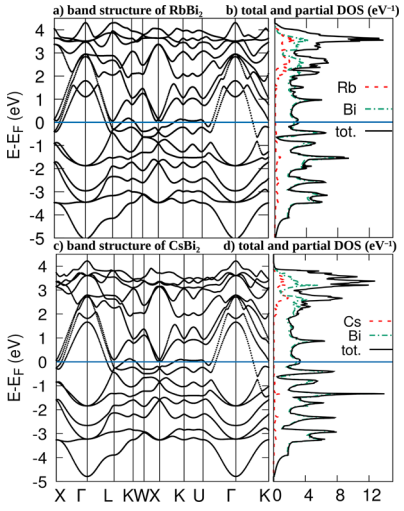

Figure 5. Fully relativistic electronic band structure (a,c) and DOS (b,d) of $RbBi_2$ and $CsBi_2$, respectively. Atomic contributions to DOS are marked with green (Bi) and red (Rb/Cs) lines.

Table 1. Normal and Superconducting State Parameters for $RbBi_2$ and $CsBi_2$

	$RbBi_2$	$CsBi_2$
γ (mJ mol^{-1}K^{-2})	5.0(4)	4.9(2)
β (mJ mol^{-1}K^{-4})	2.83(3)	3.11(5)
Debye temp. Θ_D (K)	127(1)	123(1)
critical temp. T_c (K)	4.25	4.65
$\Delta C_p/\gamma T_c$	2.03	2.63
λ	0.82	0.87
$H_c(0)$ (Oe)	188(1)	196(5)

eV^{-1}/f.u.) than $RbBi_2$ (DOS(E_F) = 1.31 eV^{-1}/f.u.), which is correlated with a higher transition temperature T_c, as discussed below.

The plot of DOS shows that the *p*-states of Bi contribute the majority of the total DOS around the Fermi level, being only slightly hybridized with *s* states of Rb/Cs. Bi 6*s* states are positioned well below the E_F due to (scalar) relativistic effects.[3] Thus, both the metallic state and superconductivity in ABi_2 arises from interacting 6*p* states of Bi atoms. In the energy range from −2.5 to 3 eV (with respect to E_F) the shape of DOS is similar to the one of elemental bismuth. Particularly, the minimum at −0.8 eV is similar to the one at Fermi level of pure Bi. Around the E_F the peak of DOS arises similarly to the case of elemental Bi under pressure p = 2.7 GPa, at which a phase transition to a monoclinic structure is observed and Bi becomes superconducting below T_c = 3.9 K.[50] In this sense, the presence of Rb/Cs atoms impose a chemical pressure on the lattice of Bi atoms, leading to stronger 6p orbital overlap and metallic bonding of the Bi framework.

Since the density of states is around the Fermi level is dominated by the Bi_4 pyrochlore lattice, relativistic effects have a profound effect on the electronic structure. In Figure 6, the scalar and fully relativistic band structure is shown in a narrow energy range around E_F. In the case of $RbBi_2$, when SOC is not included, the Fermi level is positioned in the flat part of DOS, while with SOC, the local maximum appears and the Fermi level is situated on its slope.

The parabolic bands around Γ point with a large (3 eV) energy gap around the Fermi level are not affected by SOC. At many points of *k*-space (for example between *K* and *U* or *X* and Γ points), mainly below the Fermi level, the band crossings are removed by SOC.

Figure 7 shows the Fermi surface (FS) of $RbBi_2$ and $CsBi_2$ calculated with and without SOC. Since the differences in FS between the two compounds are negligible, we will discuss the $RbBi_2$ case only. The only difference between the two compounds lies in the Fermi velocity which is slightly smaller in the case of $CsBi_2$ in the [1 0 0] direction. This is consistent with a less dispersed character of bands around E_F and a higher DOS at the Fermi level of this compound.

In the scalar relativistic case, there are four bands per spin crossing the E_F, and thus four FS branches. First one (I in Figure 7a,d) has a dodecahedral shape with almost completely flat faces. It is similar to the Fermi surface of polonium which was concluded to lead to strong nesting.[51−53] The hybridization causes the presence of cone-like corners. Additionally, there are small pockets around *K* and *U* points. This part of the Fermi surface is associated with the band which is approximately parabolic around the Γ point. The second branch (II) contains many cylinders and is associated with a flat band at the *K*−*U* line. The third and fourth branches of the Fermi surface (III and IV in Figure 7a,d) consist of small pockets centered at *X* and *L* points. At the *X* point, all four bands degenerate to two points, both ca. 0.5 eV below the Fermi level. The SOC shifts them leaving one below and one above the E_F. In the fully relativistic case, the Fermi surface is reduced to just two branches: the dodecahedral and the cylindrical one, both centered at Γ. Small conical pockets of branch I are removed.

MOST WIEDZY Downloaded from mostwiedzy.pl

https://doi.org/10.1021/acs.jpcc.3c02176
J. Phys. Chem. C 2023, 127, 14402−14414

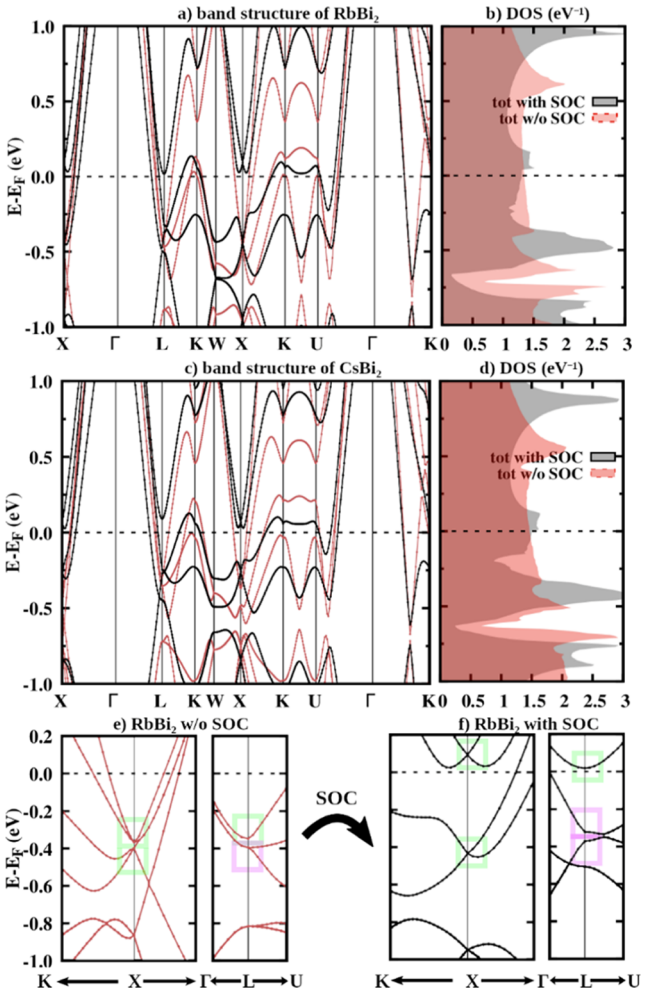

Figure 6. Electronic band structure (a,c) and DOS (b,d) of $RbBi_2$ and $CsBi_2$, respectively, calculated in a scalar- (without SOC; red line) and fully relativistic approach (with SOC; black). Panels (e,f) show the band structure around the Brillouin zone center (Γ) for $RbBi_2$. At the *X* point, the degeneracy is symmetry-protected, so the inclusion of SOC results only in shifting the band energies (points marked with green rectangles), while at *L*-point they are additionally split (purple rectangles).

The degeneracy of bands at *X*-point is symmetry-enforced and leads $RbBi_2$ and $CsBi_2$ to be classified topologically as ESFD (enforced semimetals with Fermi degeneracy).[54] The two compounds might be interesting for studying the interplay of superconductivity and topologically nontrivial states. Despite the vanishing FS pockets and the change in the general shape of DOS function around the Fermi level, the value of DOS at the E_F of $RbBi_2$ is almost unchanged by SOC (a negligible decrease from 1.35 to 1.31 eV^{-1}/f.u. is seen). The reduction of the number of FS branches is compensated by the reduction of the Fermi velocity (see Figure 7a,b), as lower velocity leads to a higher density of states.

Since the electronic structure is strongly affected by the inclusion of the spin−orbit coupling, it is interesting how the changes are reflected in the vibrational structure. Calculated phonon band structures of $RbBi_2$ and $CsBi_2$ are shown in Figure 8 and 9. In contrast to the electronic structure, the phonon dispersion curves (Figures 8a,d and 9a,d) and density of states (Figures 8c,f and 9c,f) of the two compounds differ significantly.

The SOC has a major influence on phonons. When it is not taken into account, the vibrational structure of $RbBi_2$ is rich in softened modes, suggesting the instability of the structure. When SOC is included, the softening of modes disappears, indicating a stabilization by relativistic effects. This is consistent with the lack of period 5 pyrochlore analogues of $RbBi_2$ and $CsBi_2$ (e.g., $RbSb_2$ is a semiconductor with a monoclinic structure[55]), as relativistic effects, stabilizing the perfect pyrochlore lattice, are much weaker in Sb.

The phonon spectrum contains 18 modes, as the primitive cell of $RbBi_2$ contains six atoms (2 formula units). Phonon modes coming from Bi and Rb atomic vibrations are not strongly separated from each other as it is, e.g., in the case of LiBi[8] or $CaBi_2$.[14] However, the three acoustic modes and low-frequency optic modes (up to ω = 1.7 THz) are mainly associated with Bi atoms vibrations, while high-frequency modes (in the range ω = 1.7−2.5 THz) come mostly from Rb. Transverse acoustic (TA) modes degenerate along the *X*−Γ−*L* path and split in the *xy* plane along *W*−Γ−*K*. The optical modes coming from Bi lie within a narrow frequency range ω = 1.1 to 1.4 THz and a part of them is almost flat, resulting in a peak in the phonon DOS. The exception is the highest mode, which is the breathing mode of a pyrochlore network[56−59] associated with a movement of Bi atoms toward the center of the tetrahedron and breaking of the inversion symmetry of the lattice (see Figure 9e).

The vibrations of atoms along the line, as in case of this mode is only a special case of trajectory of atoms, generally described by formula

$$\mathbf{r}_s(t) = \mathrm{Re}(\widehat{\epsilon_{\nu s}}\exp(i(\mathbf{q}\cdot\mathbf{R} - \omega_\nu t))) = \mathrm{Re}(\widehat{\epsilon_{\nu s}})\cdot\cos(\omega_\nu t + \mathbf{q}\cdot\mathbf{R}) + \mathrm{Im}(\widehat{\epsilon_{\nu s}})\cdot\sin(\omega_\nu t + \mathbf{q}\cdot\mathbf{R})$$

where $\mathbf{r}_s(t)$ is the position of atom s in time t, with crystallographic position $\mathbf{R}$, $\widehat{\epsilon_{\nu s}}$ is its polarization vector associated with phonon mode ν with frequency ω_ν and all is considered in the $\mathbf{q}$-point of the space of wave vectors.

With one of the part (real or imaginary) of polarization vector equal to zero, atoms vibrate along the line with frequency ω and direction given by the polarization vector. When both parts are non-zero, the atomic trajectory is an ellipsoid. If additionally both parts are equal, the ellipsoid becomes a circle. Such a case has been found in many $\mathbf{q}$ points of phonon dispersion of $RbBi_2$. Two examples are shown in Figure 8h,i. At the *K* point, Rb atoms are moving circularly, while Bi atoms move along a line. At the *W* point, all atoms are moving along a circle/ellipse (see the animation of the atomic vibrations in the Supporting Information). These modes might be candidates for chiral phonons which arise due to symmetry of the crystal structure and have been recently found in ABi compounds, including RbBi and CsBi[60] (the occurrence of chiral phonons in ABi_2 compounds is discussed in more detail in ref 61).

The phonon spectrum of $CsBi_2$ is qualitatively different from $RbBi_2$. When SOC is neglected, the modes are not only softened as it is in the case of $RbBi_2$ but the spectrum is also rich in imaginary frequencies, suggesting structural instability. Inclusion of the SOC removes the imaginary frequencies; thus, the relativistic effect of SOC is crucial for the stability of the cubic Laves structure of $CsBi_2$.

As visualized in Figure 9, the soft mode is associated with a movement of Bi atoms toward the center of faces of tetrahedron. As is highlighted in the electronic charge density

MOST WIEDZY Downloaded from mostwiedzy.pl

https://doi.org/10.1021/acs.jpcc.3c02176
J. Phys. Chem. C 2023, 127, 14402−14414

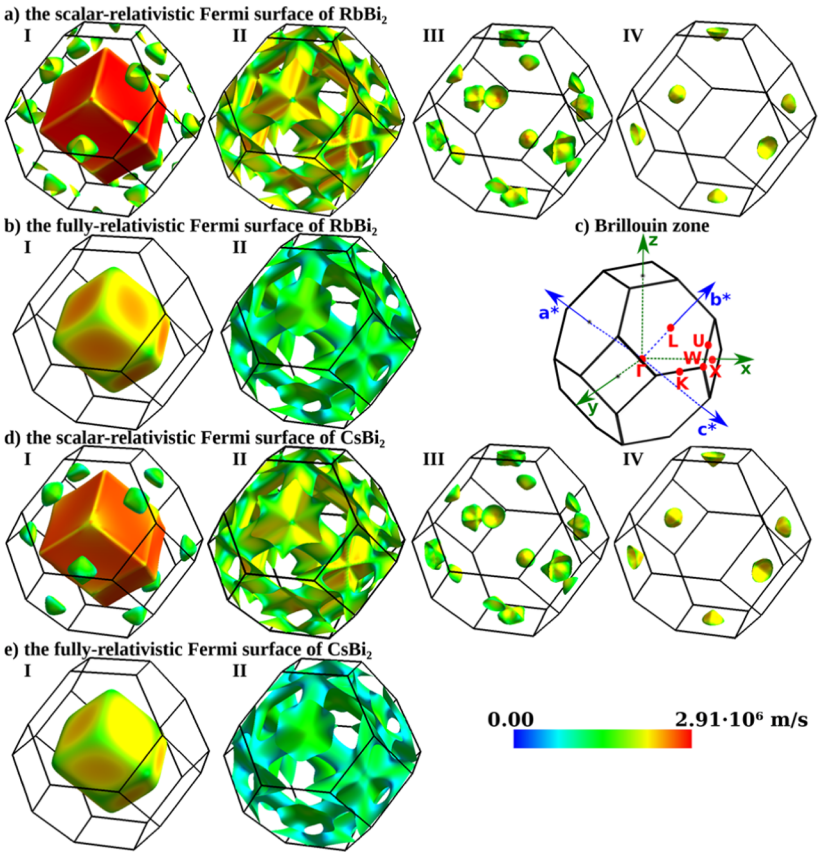

Figure 7. Fermi surface of $RbBi_2$ (a,b) and $CsBi_2$ (d,e) calculated without SOC (a,d) and with SOC (b,e), colored according to Fermi velocity. The Brillouin zone with high symmetry points is shown in panel (c).

plot (Figure 4b), this point is characterized by large electronic charge density associated with metallic bonds of close-packed Bi tetrahedron. Thus, this mode may be seen as movement of positively charged Bi ions, which are attracted to the region of a large, negative charge density, leading to lowering of frequency.

When SOC is included, the p orbital is contracted; thus, the metallic bonds are slightly weakened and the electronic density on the faces of tetrahedra is reduced (see Figure S6 of the Supporting Information, where the difference of electronic charge density, calculated with and without SOC, is presented). This leads to the changes in the vibrational structure: the Bi atoms move in different direction and the imaginary frequencies disappear. As we checked, similar change of displacement vectors of atoms is associated with the disappearance of softened modes of $RbBi_2$. This behavior may suggest that the softening arises from a Kohn anomaly caused by an electronic effect of nesting of the Fermi surface, which would be an interesting matter of further studies.

The influence of electronic surrounding on phonons is highlighted by a large phonon linewidth of discussed modes, shown in Figures 8a and 9a in a fat band representation. It is defined as

$$\gamma_{\mathbf{q}\nu} = 2\pi\omega_{\mathbf{q}\nu}\sum_{ij}\int\frac{d^3k}{\Omega_{BZ}}|g_{\mathbf{q}\nu}(\boldsymbol{k}, i, j)|^2 \times (E_{\boldsymbol{k}j} - E_F)\delta(E_{\boldsymbol{k}+\mathbf{q},i} - E_F)$$

where electron−phonon coupling matrix element

$$g_{\mathbf{q}\nu}(\boldsymbol{k}, i, j) = \sum_s\sqrt{\frac{\hbar}{2M_s\omega_{\mathbf{q}\nu}}}\langle\psi_{i,\boldsymbol{k}+\mathbf{q}}\left|\frac{dV_{SCF}}{d\hat{u}_{\nu s}}\cdot\hat{e}_{\nu s}\right|\psi_{j\boldsymbol{k}}\rangle$$

describes how the electronic potential is changed by an atomic displacement, $\omega_{q\nu}$ is a frequency of the ν-th mode with a wave vector $\mathbf{q}$ (equal to a difference of wave vectors of two electronic states $\psi_{i,k+q}\psi_{jk}$) with a polarization vector $\hat{e}_{\nu s}$, associated with a displacement $\hat{u}_{\nu s}$ of s-th atom of a mass M_s. Dirac delta functions ensure that only the electronic states near the FS are included in calculation.

On the other hand, the EPC matrix influences the electron−phonon part of dynamical matrix, given by[62]

$$\Phi^{EP}(q)_{\kappa\alpha\kappa'\alpha'} = \frac{2}{N}\sum_{nn'k}\frac{f_{k+q,n} - f_{k,n}}{E_{k+q,n'} - E_{k,n}}(g_{q\nu}(k, i, j)^*)^{k\alpha}(g_{q\nu}(k, i, j))^{\kappa'\alpha'}$$

where $E_{k,n}$ and $f_{k,n}$ are energy and occupancy of the n-th band at k-th point, N is a number of unit cells. The phonon frequencies are the eigenvalues of the dynamical matrix normalized by atomic masses. In consequence, the higher value of the EPC matrix leads to lower frequency. As a consequence, the phonon softening and phonon linewidth are associated with each other, as both depend on the EPC matrix and geometry of FS. It is visible in Figures 8a and 9a, where the softened modes are characterized by large phonon linewidth.

It is worth noting that not all softened modes disappeared with SOC. Many of softened optical modes survived and their large phonon linewidth demonstrates that their softening is

MOST WIEDZY Downloaded from mostwiedzy.pl

https://doi.org/10.1021/acs.jpcc.3c02176
J. Phys. Chem. C 2023, 127, 14402−14414

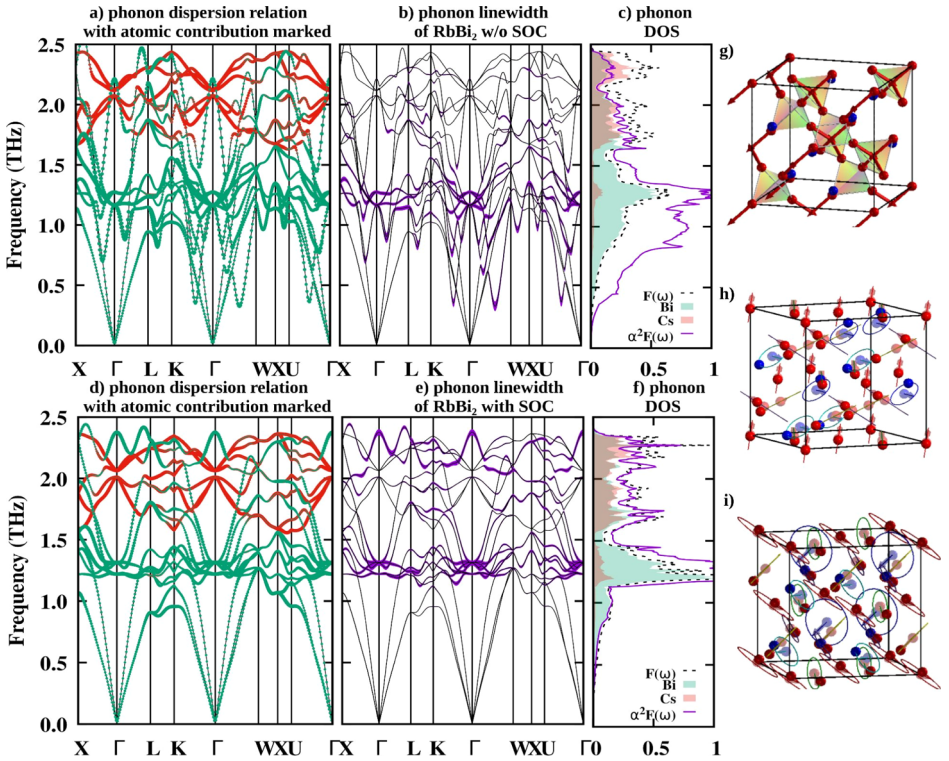

Figure 8. Panels (a,b,d,e): phonon dispersion relation of $RbBi_2$ with phonon linewidth proportional to the thickness of the purple line. Panels (c,f) show the phonon DOS (dashed black line) with atomic contribution marked in green (Bi) and red (Rb) and the Eliashberg function (purple line) normalized to $3N$ (N being a number of atoms per unit cell), calculated without SOC (a−c) and with SOC (d−f). In panel (g), the vibrational direction associated with the highest mode at Γ is marked with arrows attached to atoms of elementary crystal cell (in real space). Similarly, the trajectory of atoms associated with two examples of possible chiral modes: second mode at K and fifth at W are shown in panels (h,i). The Rb and Bi atoms are marked with blue and red spheres, respectively.

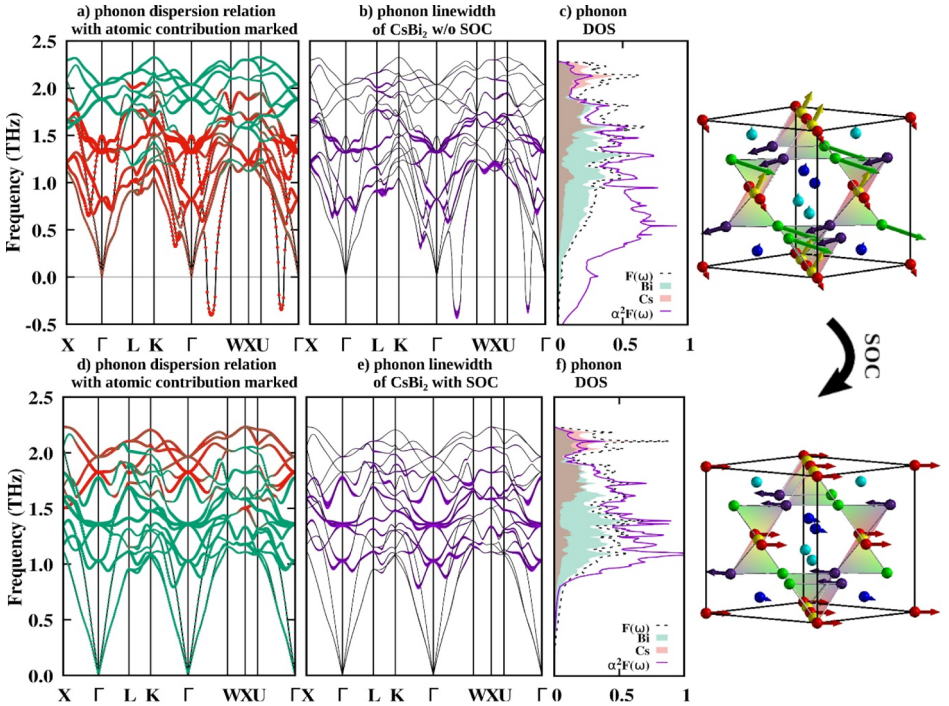

Figure 9. Phonon dispersion relation of $CsBi_2$ together with phonon linewidth (a,b,d,e) and its phonon DOS together with atomic contribution to phonon DOS and Eliashberg function, calculated w/o SOC (a−c) and with SOC (d−f). The color scheme is the same as in Figure 8. The soft mode, which appears along Γ−W in the scalar-relativistic case, is marked in real space with arrows (yellow, red, green, and purple balls are Bi, and light and dark blue are Cs).

MOST WIEDZY Downloaded from mostwiedzy.pl

https://doi.org/10.1021/acs.jpcc.3c02176
J. Phys. Chem. C 2023, 127, 14402−14414

due to strong EPC, showing their importance for superconductivity. This is an important factor in the formation of the superconducting state, as the inclusion of SOC stabilizes the phonon structure to the point where the compound becomes dynamically stable, but softened modes provide a sizable contribution to the electron−phonon coupling.

The influence of SOC on ABi_2 family is similar to the case of other family of Bi-rich superconductors, ABi_3, which crystallize in a simple cubic $AuCu_3$-type structure, within which all the A−Bi and Bi−Bi distances are equal. In the case of lighter $SrBi_3$, the SOC only removes softened modes with large phonon linewidth, while in the case of heavier $BaBi_3$, it also stabilizes the structure. In addition, both Ba- and Bi-derived modes of $BaBi_3$ are lower than in the case of $SrBi_3$, leading to nearly 30% larger value of EPC constant, which is equal to 1.43 and 1.11, respectively.[16] In the ABi_2 family, the substitution of lighter Rb with heavier Cs leads to only about 10% larger EPC constant.

Modes associated with Cs atoms have lower frequency than those associated with Rb (average frequency of Cs is 9% lower than that of Rb, see Table 2). This is expected since Cs is over 55% heavier than Rb. The average frequency of Bi is of 5% lower in $CsBi_2$ than in $RbBi_2$. Surprisingly, not all modes of Bi are lowered leading to a completely different shape of phonon DOS, where the peak around 1.3 THz is spread out.

Table 2. Summary of Calculated Properties of $RbBi_2$ and $CsBi_2$ Compared to Experimental Results (Marked with Label Expt)[a]

	$RbBi_2$		$CsBi_2$	
	w/o SOC	w. SOC	w/o SOC	w. SOC
$N(E_F)$/f.u.	1.35	1.31	1.46	1.51
λ_{expt}	0.82		0.87	
λ	2.06	0.81		0.92
$\bar{\omega}$	1.59	1.61		1.51
	Rb: 1.91	Rb: 1.85		Cs: 1.69
	Bi: 1.36	Bi: 1.45		Bi: 1.38
ω_{ln}	0.85	1.74		1.27
T_c	6.18	3.31		3.85
T_c (expt.)	4.24		4.65	

[a]The density of states is given in units of eV^{-1}/f.u., both mean frequency $\bar{\omega}$ and logarithmic frequency ω_{ln} in units of THz and critical temperatures in K.

In order to better describe the difference between the phonon structures of $CsBi_2$ and $RbBi_2$, dispersion relations around the Γ point are plotted and the modes associated with similar movement of atoms are marked with the same color in Figure 10. Additionally, modes associated with the movement of Bi atoms are visualized in Figure 10c−f and force constants between atoms are shown in Figure 10g. The modes associated with a movement of both Bi (along Bi−Bi bond) and Cs/Rb (Figure 10d) are lowered from 1.31 in the case of $RbBi_2$ to 1.03 THz in $CsBi_2$, while the frequency of modes associated with a movement of Bi toward the empty space around Cs/Rb (Figure 10c,e) are increased from 1.22 THz and 1.32 THz in $RbBi_2$ to 1.36 THz in $CsBi_2$.

This may be caused by a difference in the unit cell size, which is larger in the case of $CsBi_2$; thus, the Bi−Bi metallic bonding is slightly weaker leading to smaller force constants of Bi−Bi pairs (see Figure 10h) and lower frequencies of modes associated with a movement of Bi along Bi−Bi bonds. For the same reason, the highest optical mode associated with a movement of Bi toward the center of tetrahedron (Figure 10f) is lowered from 2.37 THz in the case of $RbBi_2$ to 1.78 THz in $CsBi_2$. It is similar to the case of soft mode shown in Figure 9e and explains why the effect of softening is stronger in the case of $CsBi_2$. On the other hand, the force constants of Bi−Cs pairs are larger than of Bi−Rb pairs, leading to a higher frequencies of modes associated with movements of Bi toward the space around Cs. These changes show that the substitution of Rb by Cs not only lowers the frequency due to a larger mass but also influences the size of the unit cell and modifies the bonding of the Bi network.

In both compounds, the phonon linewidths are large only in case of Bi modes. Since the FS is also dominated by 6*p* states of Bi, the superconductivity in ABi_2 is driven by the Bi pyrochlore lattice, as the electron−phonon coupling in both electronic and phonon ways is almost exclusively contributed by Bi.

On the basis of the phonon linewidth, the Eliashberg function is calculated

$$\alpha^2F(\omega) = \frac{1}{2\pi N(E_F)} \sum_{q\nu} \delta(\omega - \omega_{q\nu}) \frac{\gamma_{q\nu}}{\hbar\omega_{q\nu}}$$

The Eliashberg function is effectively the phonon DOS weighted by a phonon linewidth divided by phonon energy and density of electronic states at the Fermi level.

Eliashberg function of $RbBi_2$, calculated without SOC, is the highest at low frequencies (up to 1.5 THz) due to the presence of softened acoustic modes and low-frequency optical modes. When SOC is included, the Eliashberg function becomes similar to phonon DOS, which means that electron−phonon coupling only weakly depends on phonon frequency. The largest contribution to Eliashberg function comes from highly degenerate and partially flat Bi modes in the narrow frequency range.

Having the Eliashberg function, we can calculate the electron−phonon coupling constant

$$\lambda = 2 \int_0^{\omega_{max}} \frac{\alpha^2F(\omega)}{\omega} d\omega$$

It is essentially proportional to phonon linewidth divided by frequency squared; thus, the low frequency modes contribute more than higher ones. Obtained values are shown in Table 2. When SOC is not included, the EPC constant of $RbBi_2$ λ = 2.06, is more than twice larger than the experimental value (Table 1). The cumulative EPC constant shown in Figure 11 clearly shows that such a high value is caused by softened modes, having low frequency and large phonon linewidth. When SOC is included, the softening disappears and the EPC constant decreases to λ = 0.81 in excellent agreement with the value estimated from the experiment λ = 0.82 and is mostly delivered by acoustic and optical Bi modes, as =0.82 and is mostly delivered by acoustic and optical Bi modes, as the phonon linewidth is the highest for these modes. The calculated EPC constant of $CsBi_2$ λ_{ep} = 0.92 is also in a good agreement with the experimental value λ_{ep} = 0.87. It is slightly larger than in case of $RbBi_2$ due to a shift of part of modes to lower frequencies and slight changes in band structure.

The impact of the electronic structure on EPC can be measured using the integral

MOST WIEDZY Downloaded from mostwiedzy.pl

https://doi.org/10.1021/acs.jpcc.3c02176
J. Phys. Chem. C 2023, 127, 14402−14414

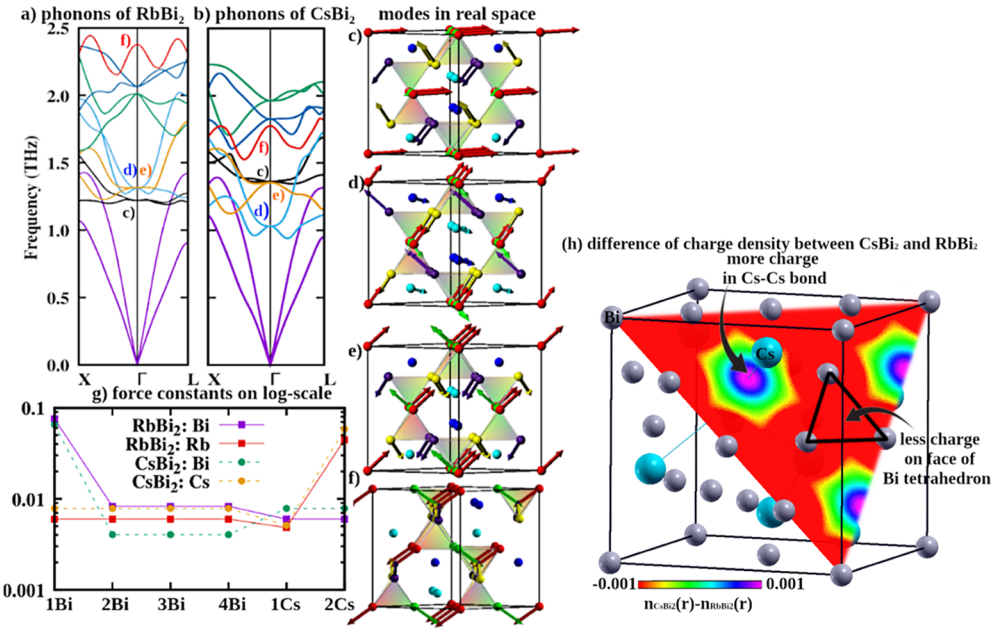

Figure 10. Phonon dispersion relation of $RbBi_2$ (a) and $CsBi_2$ (b) calculated with SOC and visualization of modes at $\mathbf{q} = (0, 0, 0)$ in real space (c–f) using the same color scheme as in Figure 9. Additionally, the force constants between nearest pairs of atoms are shown in panel (g). The unit cell contains two formula units; thus, there are four atoms of Bi and two atoms of Cs. The force constants of Bi–Bi pairs are weaker in $CsBi_2$ than $RbBi_2$, while Cs–Cs force constants are stronger than Rb–Rb. In panel (h), the difference of electronic charge density between the case of $CsBi_2$ and $RbBi_2$ is shown and the strengthening of the Cs–Cs bond in comparison to Rb–Rb together with weakening of Bi–Bi bonding in $CsBi_2$ in comparison to $RbBi_2$ is visible. As argued, it is a result of a larger unit cell, which leads to weaker Bi–Bi bonding, while Cs atoms, being larger than Rb, are bonded stronger in agreement with Bader analysis, which shows weaker ionization of Cs atoms than Rb atoms $[Rb^{+0.71}(Bi_2)^{-0.71}$ vs $Cs^{+0.64}(Bi_2)^{-0.64}]$.

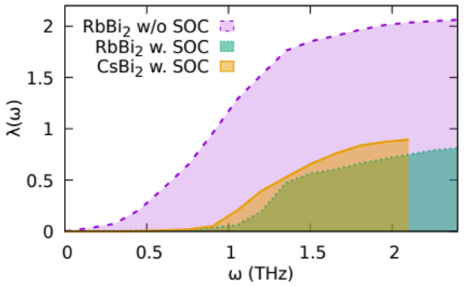

Figure 11. Cumulative EPC constant of $RbBi_2$ and $CsBi_2$.

$$I = \int_0^{\omega_{max}} \alpha^2 F(\omega) \cdot \omega \, d\omega$$

Which does not depend on phonon frequency, as

$$I = \frac{1}{N(E_F)} \sum_{i,j} \int \frac{d^3k}{\Omega_{BZ}} \left| \sum_s \frac{1}{\sqrt{2M_s}} \left\langle \psi_{i,k+q} \left| \frac{dV_{SCF}}{d\widehat{u_{\nu s}}} \right| \psi_{j,k} \right\rangle \right|^2 \cdot \delta(E_{ki} - E_F)\delta(E_{k+q,j} - E_F)$$

In a monoatomic case, this integral is closely related to the McMillan–Hopfield parameter. The calculated values of the integral are 0.90 and 1.26 THz^2 for $RbBi_2$ and $CsBi_2$, respectively. This suggests that, in addition to the lowering of frequency, the slight changes of the electronic structure resulting in lowering the Fermi velocity and increased DOS(E_F) strengthen the EPC.

On the basis of calculated EPC constant the critical temperature can be calculated with the help of the Allen–Dynes equation[63]

$$T_c = \frac{\omega_{ln}}{1.20} \exp\left(-\frac{1.04(1 + \lambda)}{\lambda - \mu^*(1 + 0.62\lambda)} \right)$$

where

$$\omega_{ln} = \exp\left(\frac{\int_0^{\omega_{max}} \alpha^2 F(\omega) \ln(\omega) \frac{d\omega}{\omega}}{\int_0^{\omega_{max}} \alpha^2 F(\omega) \frac{d\omega}{\omega}} \right)$$

is a logarithmic average of frequency. In the case of $RbBi_2$, λ = 0.81 and ω_{ln} = 1.74 THz (equivalent to 83.5 K) leading to T_c = 3.23 K (the standard value of μ^* = 0.1 is assumed), reasonably close to the measured value 4.24 K, considering that even a small underestimation of the electron–phonon coupling parameter has a profound effect on the estimated T_c. In the case of $CsBi_2$, EPC constant in larger λ = 0.92 leading to higher T_c = 3.85 K despite of lower logarithmic frequency. The estimated critical temperature is reasonably close to the experimental value T_c = 4.65 K. Both experimental and calculated values lead to a conclusion that $CsBi_2$ has higher critical temperature than $RbBi_2$ due to slightly stronger electron–phonon coupling.

In summary, the structural arrangement of Bi atoms into a pyrochlore network of Bi tetrahedra intercalated with alkali metal atoms, resulting in a relatively high electron–phonon coupling constant. This emerges as a combination of both aforementioned factors: the large electronic density within the close-packed Bi atoms in Bi_4 tetrahedra allows for the strong interaction of phonon modes with electrons (large phonon linewidths), whereas the tetrahedra themselves are relatively loosely packed within the unit cell with a large amount of "free space" filled only by Rb/Cs atoms. This, in combination with high atomic mass of Bi, results in relatively low Bi phonon

MOST WIEDZY Downloaded from mostwiedzy.pl

https://doi.org/10.1021/acs.jpcc.3c02176
J. Phys. Chem. C 2023, 127, 14402–14414

frequencies, enhancing the EPC. Recently, we discussed a similar situation in isostructural Laves phase superconductors: $SrRh_2$ and $SrIr_2$, where the pyrochlore lattice or Rh/Ir was found to be responsible for the emergence of strong-coupling superconductivity.[59]

On the other hand, $RbBi_2$ and $CsBi_2$ are in contrast with $CaBi_2$, which crystallizes in an orthorhombic structure that can be viewed in a distorted Laves phase structure, in which tetrahedra are broken to Bi−Bi and Ca−Bi planes separated from each other. Here, the phonon linewidths are smaller and average Bi frequencies are higher, leading to the EPC constant $\lambda_{ep} = 0.54$, much lower than $\lambda_{ep} = 0.82$ and $\lambda_{ep} = 0.87$ for $RbBi_2$ and $CsBi_2$, respectively, despite the value of $I = 1.17$ THz^2 lying between $RbBi_2$ and $CsBi_2$ cases. This results in a lower critical temperature ($T_c = 2.0$ K for $CaBi_2$).[13,14]

Electron population analysis on $RbBi_2$ shows that the DOS(E_F) is contributed mostly by electrons occupying nearest-neighbor Bi−Bi antibonding states (see Figure S4 of the Supporting Information). A hypothetical neutral Bi pyrochlore lattice would have its E_F lying close to a pseudogap. The electrons donated by Rb increase the antibonding population, destabilizing the lattice. Unfortunately, with the currently available computational tools (either direct in case of local basis set or indirect—via projection of plane-wave wave functions to a local orbitals set[64−67]), the bonding population analysis can only be performed in a scalar-relativistic case. While for bonding of lighter elements, SR approximation is reasonably applicable, the chemical bonding in 6th and 7th period elements is heavily influenced by SOC effects.[68,69] A possible solution for reliable population analysis of compounds of the heaviest elements is via the localized Wannier spinors.[70]

The calculated electronic structure of the Bi_4 cluster (shown in Figure 12) are in general consistent with the previous results

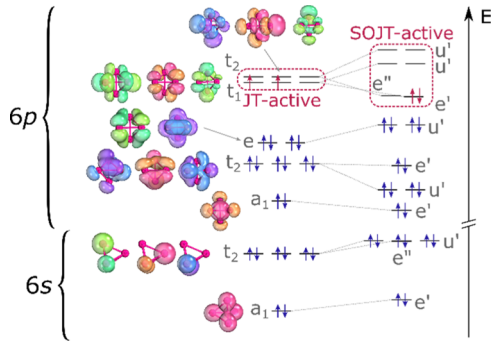

Figure 12. Molecular orbitals of a tetrahedral Bi_4 cluster. Note that for clarity of the picture, the energy scale (right) is divided into two parts, as the separation between lower t_2 and higher a_1 levels is on the order of 8 eV, while for comparison the t_2−e splitting is ca. 0.5 eV.

by Lohr and Pyykkö obtained by means of relativistically parametrized extended Hückel method,[71] although the ordering of virtual orbitals is slightly different. The stabilizing effect of SOC on ABi_2 can be qualitatively understood by considering the electronic structure of a T_d Bi_4 cluster. First, in a heavy element, such as Bi, scalar-relativistic effects result in a complete energetic separation of 6*s* and 6*p* orbitals.[3] Thus, only the p orbitals participate in the bonding. Second, the SOC splits the 6*p* atomic level into $p_{1/2}$ and $p_{3/2}$ separated by ca. 2 eV in a free atom. In the scalar-relativistic approximation the neutral Bi_4 cluster is a closed-shell system with four electrons occupying the doubly degenerate *e* HOMO level. With two additional electrons donated by electropositive species, the Bi_4^{2-} is first-order Jahn−Teller (JT) active due to two electrons occupying a triply degenerate t_1 level. SOC splits the 6*p*-derived levels (6*s*-derived lower t_2 level is also weakly split due to small admixture of the *p* character), lifting the triple degeneracy of t_1 and t_2. The two additional electrons now occupy a e' (Γ_6) level, quasi-degenerate ($\Delta E \approx 0.02$ eV) with the next e'' (Γ_7) leading to structural stabilization. However, the splitting of the e' and the two u' (Γ_8) levels is relatively small ($\Delta E \approx 0.9$ and 1.2 eV, respectively), resulting in a possibility of a second-order JT instability, as pointed out by Lohr and Pyykkö.[71] While the electronic structure of the crystalline ABi_2 compound is much more complex than of isolated cluster, the stabilizing effects of SOC similarly stem from the lifted p orbital degeneracy, while the weakened but persistent mode softening can be considered an effect of a second-order JT (SOJT) effect.

This observation suggests a criterion for finding new superconductors: one may look for compounds stabilized by strong SOC, which should show relatively strong electron−phonon coupling while avoiding crystal structure distortion. Examples of such SOC stabilized superconductors can be found among Sb-, Bi-, and Pb-rich intermetallic phases featuring hypervalent polyanions, listed in Table 3. The

Table 3. Superconductors Featuring Sb-, Te-, Bi-, and Pb-Based Hypervalent Polyanions

material	hypervalent network	T_c
Ba_3TiTe_5	1d Te^- chains	6 K (p = 37 GPa)[75]
$YbSb_2$	2d Sb^- square network	1.3 K[47,76]
LiBi	2d Bi^- square network	2.5 K[8,19]
NaBi	2d Bi^- square network	2.15 K[7]
$CaBi_2$	2d Bi^- square network	2.0 K[13]
$Ba_2Bi(Bi_xSb_{1-x})_2$	2d Sb/Bi "square-honeycomb"	max. 4.4 K[18,77]
$LaPb_3$	3d Pb^- cubic network	4 K[78]
$LaBi_3$	3d Bi^- cubic network	7.3 K[79]

$(Bi_4)^{2-}$ pyrochlore lattice can be considered as hypervalent based on the valence electron count argument. The neutral Bi atom is three electrons short of octet, and thus, with four covalent bonds in the pyrochlore lattice, it is already electron-rich. The two electrons donated by two Rb/Cs atoms increase the electron count further, resulting in an even more hypervalent anionic network.

KBi_2, $RbBi_2$, and $CsBi_2$ belong to a large family of cubic Laves (C-15) superconductors. The SuperCon database lists 192 C-15 superconductors, belonging to 16 different chemical systems, with critical temperatures ranging from 0.7 K to 10.7 K. However, the three Bi-based compounds distinguish themselves from the whole family in a number of ways. First, besides $LaAl_2$ ($T_c \approx 3$ K)[72] and $LaMg_2$ ($T_c \approx 1$ K), they are the only main-group element-based Laves superconductors. Second, we have shown (based on electronic and vibrational structure, and electron−phonon coupling calculations) that in $RbBi_2$ and $CsBi_2$ systems, the superconductivity clearly emerges from the electron-rich Bi pyrochlore lattice, with Rb and Cs acting predominantly as electron donors to the Bi lattice. Such a clear picture cannot be drawn in the case of transition-metal-based systems, where the bonding between atoms occupying the two crystal sites is expected to be much more metallic. Lastly, Bi is the heaviest stable element ($Z = 83$) and the relativistic effects on electronic properties in KBi_2,

MOST WIEDZY Downloaded from mostwiedzy.pl

https://doi.org/10.1021/acs.jpcc.3c02176
J. Phys. Chem. C 2023, 127, 14402−14414

$RbBi_2$, and $CsBi_2$ are the strongest of all of the Laves superconductors, even when compared with Ir- and Au-based systems, such as (La/Lu)Ir_2[73] and (Pb,Bi)Au_2,[74] since the SOC effect on 5*d* valence electrons is weaker than that on the 6*p* shell.

CONCLUSIONS

We have analyzed the electronic and vibrational properties of two Bi-based cubic Laves phases: $RbBi_2$ and $CsBi_2$. Our results show that the occurrence of superconductivity in these two compounds and an isostructural KBi_2 stems almost exclusively from the heavy element pyrochlore lattice. Both the stability of the phases and their electronic and vibrational properties are heavily affected by relativistic effects. The spin−orbit coupling is crucial for the dynamic stability of $CsBi_2$, and to a lesser extent $RbBi_2$. The stability enhancement can be explained by considering an isolated Bi_4 cluster and the effects of SOC on its electronic structure. We postulate that crystal structures based on relativistically stabilized hypervalent networks of heavy elements are interesting candidates for finding new superconductors.

ASSOCIATED CONTENT

Supporting Information

The Supporting Information is available free of charge at https://pubs.acs.org/doi/10.1021/acs.jpcc.3c02176.

PXRD patterns for $RbBi_2$ and $CsBi_2$ samples; crystal unit cell parameters for $RbBi_2$ and $CsBi_2$; plot of critical field versus temperature; low-temperature heat capacity of $RbBi_2$ and $CsBi_2$; crystal orbital Hamilton population (COHP) plot for $RbBi_2$; and electronic band structure, charge density, and phonon dispersion plots for elemental Bi (PDF)

Chiral phonon animation (MP4)

AUTHOR INFORMATION

Corresponding Author

Michał J. Winiarski − *Faculty of Applied Physics and Mathematics and Advanced Materials Center, Gdansk University of Technology, 80-233 Gdansk, Poland;* orcid.org/0000-0001-9083-8066; Email: michal.winiarski@pg.edu.pl

Authors

Sylwia Gutowska − *Faculty of Physics and Applied Computer Science, AGH University of Science and Technology, 30-059 Kraków, Poland*

Bartlomiej Wiendlocha − *Faculty of Physics and Applied Computer Science, AGH University of Science and Technology, 30-059 Kraków, Poland;* orcid.org/0000-0001-9536-7216

Tomasz Klimczuk − *Faculty of Applied Physics and Mathematics and Advanced Materials Center, Gdansk University of Technology, 80-233 Gdansk, Poland;* orcid.org/0000-0002-7089-4631

Complete contact information is available at: https://pubs.acs.org/10.1021/acs.jpcc.3c02176

Author Contributions

The manuscript was written through contributions of all authors.

Notes

The authors declare no competing financial interest.

ACKNOWLEDGMENTS

We gratefully acknowledge helpful discussions with Dr. Andrzej Ptok (INP PAS, Poland). The research performed at the AGH-UST was supported by the National Science Centre (Poland), Project no. 2017/26/E/ST3/00119. S.G. was partly supported by the EU Project POWR.03.02.00-00-I004/16.

ABBREVIATIONS

COHP, crystal orbital Hamilton population; DKH2, Douglas−Kroll−Hess—second-order Douglas−Kroll−Hess relativistic correction; DOS, density of states; EPC, electron−phonon coupling; GGA, generalized gradient approximation; PBE, Perdew−Burke−Ernzerhof exchange-correlation potential; PXRD, powder X-ray diffraction; QE, Quantum Espresso package; SOC, spin−orbit coupling

REFERENCES

(1) Kanatzidis, M.; Sun, H.; Dehnen, S. Bismuth—The Magic Element. *Inorg. Chem.* **2020**, *59*, 3341−3343.

(2) *Holleman-Wiberg's Inorganic Chemistry*; Wiberg, N., Holleman, A. F., Wiberg, E., Eds.; Academic Press Inc: San Diego: Berlin; New York, 2001.

(3) Pyykkö, P. Relativistic Effects in Chemistry: More Common Than You Thought. *Annu. Rev. Phys. Chem.* **2012**, *63*, 45−64.

(4) Whitmire, K. H. Bismuth: Inorganic Chemistry. In *Encyclopedia of Inorganic and Bioinorganic Chemistry*; John Wiley & Sons, Ltd., 2014; pp 1−32.

(5) Nesper, R. Structure and Chemical Bonding in Zintl-Phases Containing Lithium. *Prog. Solid State Chem.* **1990**, *20*, 1−45.

(6) A Papoian, G.; Hoffmann, R. Hypervalent Bonding in One, Two, and Three Dimensions: Extending the Zintl−Klemm Concept to Nonclassical Electron-Rich Networks. *Angew. Chem., Int. Ed.* **2000**, *39*, 2408−2448.

(7) Kushwaha, S. K.; Krizan, J. W.; Xiong, J.; Klimczuk, T.; Gibson, Q. D.; Liang, T.; Ong, N. P.; Cava, R. J. Superconducting Properties and Electronic Structure of NaBi. *J. Phys.: Condens. Matter* **2014**, *26*, 212201.

(8) Górnicka, K.; Gutowska, S.; Winiarski, M. J.; Wiendlocha, B.; Xie, W.; Cava, R. J.; Klimczuk, T. Superconductivity on a Bi Square Net in LiBi. *Chem. Mater.* **2020**, *32*, 3150−3159.

(9) Merlo, F.; Fornasini, M. L. Crystal Structure of Some Phases and Alloying Behaviour in Alkaline Earths, Europium and Ytterbium Pnictides. *Mater. Res. Bull.* **1994**, *29*, 149−154.

(10) Ovchinnikov, A.; Bobev, S. Bismuth as a Reactive Solvent in the Synthesis of Multicomponent Transition-Metal-Bearing Bismuthides. *Inorg. Chem.* **2020**, *59*, 3459−3470.

(11) Tremel, W.; Hoffmann, R. Square Nets of Main-Group Elements in Solid-State Materials. *J. Am. Chem. Soc.* **1987**, *109*, 124−140.

(12) Sturza, M.; Han, F.; Malliakas, C. D.; Chung, D. Y.; Claus, H.; Kanatzidis, M. G. Superconductivity in the Intermetallic Pnictide Compound Ca11Bi10-x. *Phys. Rev. B: Condens. Matter Mater. Phys.* **2014**, *89*, 054512.

(13) Winiarski, M. J.; Wiendlocha, B.; Gołąb, S.; Kushwaha, S. K.; Wiśniewski, P.; Kaczorowski, D.; Thompson, J. D.; Cava, R. J.; Klimczuk, T. Superconductivity in CaBi2. *Phys. Chem. Chem. Phys.* **2016**, *18*, 21737−21745.

(14) Gołąb, S.; Wiendlocha, B. Electron-Phonon Superconductivity in CaBi2 and the Role of Spin-Orbit Interaction. *Phys. Rev. B* **2019**, *99*, 104520.

(15) Iyo, A.; Yanagi, Y.; Kinjo, T.; Nishio, T.; Hase, I.; Yanagisawa, T.; Ishida, S.; Kito, H.; Takeshita, N.; Oka, K.; Yoshida, Y.; Eisaki, H. Large Enhancement of Superconducting Transition Temperature of SrBi3 Induced by Na Substitution for Sr. *Sci. Rep.* **2015**, *5*, 10089.

MOST WIEDZY Downloaded from mostwiedzy.pl

(16) Shao, D. F.; Luo, X.; Lu, W. J.; Hu, L.; Zhu, X. D.; Song, W. H.; Zhu, X. B.; Sun, Y. P. Spin-Orbit Coupling Enhanced Superconductivity in Bi-Rich Compounds ABi3 (A = Sr and Ba). *Sci. Rep.* **2016**, *6*, 21484.
(17) Haldolaarachchige, N.; Kushwaha, S. K.; Gibson, Q.; Cava, R. J. Superconducting Properties of BaBi3. *Supercond. Sci. Technol.* **2014**, *27*, 105001.
(18) Iyo, A.; Yanagi, Y.; Ishida, S.; Oka, K.; Yoshida, Y.; Kihou, K.; Lee, C. H.; Kito, H.; Takeshita, N.; Hase, I.; et al. Superconductivity at 4.4 K in Ba 2 Bi 3. *Supercond. Sci. Technol.* **2014**, *27*, 072001.
(19) Sambongi, T. Superconductivity of LiBi. *J. Phys. Soc. Jpn.* **1971**, *30*, 294.
(20) Roberts, B. W. Survey of Superconductive Materials and Critical Evaluation of Selected Properties. *J. Phys. Chem. Ref. Data* **1976**, *5*, 581−822.
(21) Dshemuchadse, J.; Steurer, W. Some Statistics on Intermetallic Compounds. *Inorg. Chem.* **2015**, *54*, 1120−1128.
(22) Lei, X.-W.; Zhang, H.-P.; Yue, C.-Y. MgIn_2: Synthesis, Crystal and Band Structure. *Chin. J. Inorg. Chem.* **2012**, *28*, 795−800.
(23) Liu, X.; Zhao, H.; Kulka, A.; Trenczek-Zając, A.; Xie, J.; Chen, N.; Świerczek, K. Characterization of the Physicochemical Properties of Novel SnS2 with Cubic Structure and Diamond-like Sn Sublattice. *Acta Mater.* **2015**, *82*, 212−223.
(24) Le Bail, A. Whole Powder Pattern Decomposition Methods and Applications: A Retrospection. *Powder Diffr.* **2005**, *20*, 316−326.
(25) Rodríguez-Carvajal, J. Recent Advances in Magnetic Structure Determination by Neutron Powder Diffraction. *Phys. B* **1993**, *192*, 55−69.
(26) Giannozzi, P.; Baroni, S.; Bonini, N.; Calandra, M.; Car, R.; Cavazzoni, C.; Ceresoli, D.; Chiarotti, G. L.; Cococcioni, M.; Dabo, I.; et al. QUANTUM ESPRESSO: A Modular and Open-Source Software Project for Quantum Simulations of Materials. *J. Phys.: Condens. Matter* **2009**, *21*, 395502.
(27) Perdew, J. P.; Burke, K.; Ernzerhof, M. Generalized Gradient Approximation Made Simple. *Phys. Rev. Lett.* **1996**, *77*, 3865−3868.
(28) Dal Corso, A. Pseudopotentials Periodic Table: From H to Pu. *Comput. Mater. Sci.* **2014**, *95*, 337−350.
(29) Dronskowski, R.; Bloechl, P. E. Crystal Orbital Hamilton Populations (COHP): Energy-Resolved Visualization of Chemical Bonding in Solids Based on Density-Functional Calculations. *J. Phys. Chem.* **1993**, *97*, 8617−8624.
(30) Steinberg, S.; Dronskowski, R. The Crystal Orbital Hamilton Population (COHP) Method as a Tool to Visualize and Analyze Chemical Bonding in Intermetallic Compounds. *Crystals* **2018**, *8*, 225.
(31) *The STUTTGART TB-LMTO-ASA program*. https://www2.fkf.mpg.de/andersen/LMTODOC/LMTODOC.html (accessed May 17, 2023).
(32) Skriver, H. L. *The LMTO Method: Muffin-Tin Orbitals and Electronic Structure*; Springer-Verlag: Berlin; New York, 1984.
(33) Perdew, J. P.; Wang, Y. Accurate and Simple Analytic Representation of the Electron-Gas Correlation Energy. *Phys. Rev. B: Condens. Matter Mater. Phys.* **1992**, *45*, 13244−13249.
(34) Repisky, M.; Komorovsky, S.; Kadek, M.; Konecny, L.; Ekström, U.; Malkin, E.; Kaupp, M.; Ruud, K.; Malkina, O. L.; Malkin, V. G. ReSpect: Relativistic Spectroscopy DFT Program Package. *J. Chem. Phys.* **2020**, *152*, 184101.
(35) Dyall, K. G. Relativistic Quadruple-Zeta and Revised Triple-Zeta and Double-Zeta Basis Sets for the 4p, 5p, and 6p Elements. *Theor. Chem. Acc.* **2006**, *115*, 441−447.
(36) Knizia, G.; Klein, J. E. M. N. Electron Flow in Reaction Mechanisms—Revealed from First Principles. *Angew. Chem., Int. Ed.* **2015**, *54*, 5518−5522.
(37) *IboView*. http://www.iboview.org/_bgBqyRo.html (accessed May 17, 2023).
(38) Gnutzmann, G.; Wilhelm Dorn, F.; Klemm, W. Das Verhalten der Alkalimetalle zu Halbmetallen. VII. Über einige A3B- und AB2-Verbindungen der schweren Alkalimetalle mit Elementen der V. Gruppe. *Z. Anorg. Allg. Chem.* **1961**, *309*, 210−225.
(39) Emmerling, F.; Längin, N.; Petri, D.; Kroeker, M.; Röhr, C. Alkalimetallbismutide ABi und ABi2 (A = K, Rb, Cs) — Synthesen, Kristallstrukturen, Eigenschaften. *Z. Anorg. Allg. Chem.* **2004**, *630*, 171−178.
(40) Kelly, F. M.; Pearson, W. B. The Rubidium Transition at ∼ 180°k. *Can. J. Phys.* **1955**, *33*, 17−24.
(41) Weir, C. E.; Piermarini, G. J.; Block, S. On the Crystal Structures of Cs II and Ga II. *J. Chem. Phys.* **1971**, *54*, 2768−2770.
(42) Cucka, P.; Barrett, C. S. The Crystal Structure of Bi and of Solid Solutions of Pb, Sn, Sb and Te in Bi. *Acta Crystallogr.* **1962**, *15*, 865−872.
(43) Lynton, E. A. *Superconductivity*; Chapman and Hall, 1971.
(44) Powell, R. L.; Clark, A. F. Definitions of Terms for Practical Superconductors. 2. Critical Parameters. *Cryogenics* **1978**, *18*, 137−141.
(45) Sun, S.; Liu, K.; Lei, H. Type-I Superconductivity in KBi 2 Single Crystals. *J. Phys.: Condens. Matter* **2016**, *28*, 085701.
(46) Svanidze, E.; Morosan, E. Type-I Superconductivity in ScGa3 and LuGa3 Single Crystals. *Phys. Rev. B: Condens. Matter Mater. Phys.* **2012**, *85*, 174514.
(47) Zhao, L. L.; Lausberg, S.; Kim, H.; Tanatar, M. A.; Brando, M.; Prozorov, R.; Morosan, E. Type-I Superconductivity in YbSb2 Single Crystals. *Phys. Rev. B: Condens. Matter Mater. Phys.* **2012**, *85*, 214526.
(48) Peets, D. C.; Cheng, E.; Ying, T.; Kriener, M.; Shen, X.; Li, S.; Feng, D. Type-I Superconductivity in Al6Re. *Phys. Rev. B* **2019**, *99*, 144519.
(49) Górnicka, K.; Kuderowicz, G.; Carnicom, E. M.; Kutorasiński, K.; Wiendlocha, B.; Cava, R. J.; Klimczuk, T. Soft-Mode Enhanced Type-I Superconductivity in LiPd2Ge. *Phys. Rev. B* **2020**, *102*, 024507.
(50) Li, Y.; Wang, E.; Zhu, X.; Wen, H.-H. Pressure-Induced Superconductivity in Bi Single Crystals. *Phys. Rev. B* **2017**, *95*, 024510.
(51) Kang, C.-J.; Kim, K.; Min, B. I. Phonon Softening and Superconductivity Triggered by Spin-Orbit Coupling in Simple-Cubic alpha-Polonium Crystals. *Phys. Rev. B: Condens. Matter Mater. Phys.* **2012**, *86*, 054115.
(52) Min, B. I.; Shim, J. H.; Park, M. S.; Kim, K.; Kwon, S. K.; Youn, S. J. Origin of the Stabilized Simple-Cubic Structure in Polonium: Spin-Orbit Interaction versus Peierls Instability. *Phys. Rev. B: Condens. Matter Mater. Phys.* **2006**, *73*, 132102.
(53) Verstraete, M. J. Phases of Polonium via Density Functional Theory. *Phys. Rev. Lett.* **2010**, *104*, 035501.
(54) Bradlyn, B.; Elcoro, L.; Cano, J.; Vergniory, M. G.; Wang, Z.; Felser, C.; Aroyo, M. I.; Bernevig, B. A. Topological Quantum Chemistry. *Nature* **2017**, *547*, 298−305.
(55) Petri, D.; Röhr, C. $RbSb_2$ − Eine mit KSb_2 verwandte Zintl-Phase. *Z. Anorg. Allgem. Chem.* **2008**, *634*, 1724−1728.
(56) Engelkemier, J.; Fredrickson, D. C. Chemical Pressure Schemes for the Prediction of Soft Phonon Modes: A Chemist's Guide to the Vibrations of Solid State Materials. *Chem. Mater.* **2016**, *28*, 3171−3183.
(57) Schuck, G.; Kazakov, S. M.; Rogacki, K.; Zhigadlo, N. D.; Karpinski, J. Crystal Growth, Structure, and Superconducting Properties of the beta-Pyrochlore KOs2O6. *Phys. Rev. B: Condens. Matter Mater. Phys.* **2006**, *73*, 144506.
(58) Bzdušek, T.; Rüegg, A.; Sigrist, M. Weyl Semimetal from Spontaneous Inversion Symmetry Breaking in Pyrochlore Oxides. *Phys. Rev. B: Condens. Matter Mater. Phys.* **2015**, *91*, 165105.
(59) Gutowska, S.; Górnicka, K.; Wójcik, P.; Klimczuk, T.; Wiendlocha, B. Strong-Coupling Superconductivity of SrIr2 and SrRh2: Phonon Engineering of Metallic Ir and Rh. *Phys. Rev. B* **2021**, *104*, 054505.
(60) Skórka, J.; Kapcia, K. J.; Jochym, P. T.; Ptok, A. Chiral Phonons in Binary Compounds ABi (A = K, Rb, Cs) with P21/c Structure. *Mater. Today Commun.* **2023**, *35*, 105888.
(61) Basak, S.; Piekarz, P.; Ptok, A. Chiral Phonon in the Cubic System Based on the Laves Phase of ABi2 (A= K, Rb, Cs). **2022**, arXiv:2208.14041. arXiv preprint.

MOST WIEDZY Downloaded from mostwiedzy.pl

(62) Heid, R.; Pintschovius, L.; Reichardt, W.; Bohnen, K.-P. Anomalous Lattice Dynamics of Ruthenium. *Phys. Rev. B: Condens. Matter Mater. Phys.* **2000**, *61*, 12059−12062.
(63) Allen, P. B.; Dynes, R. C. Transition temperature of strong-coupled superconductors reanalyzed. *Phys. Rev. B* **1975**, *12*, 905.
(64) Maintz, S.; Deringer, V. L.; Tchougréeff, A. L.; Dronskowski, R. Analytic Projection from Plane-Wave and PAW Wavefunctions and Application to Chemical-Bonding Analysis in Solids. *J. Comput. Chem.* **2013**, *34*, 2557−2567.
(65) Maintz, S.; Deringer, V. L.; Tchougréeff, A. L.; Dronskowski, R. LOBSTER: A Tool to Extract Chemical Bonding from Plane-Wave Based DFT. *J. Comput. Chem.* **2016**, *37*, 1030−1035.
(66) Segall, M. D.; Shah, R.; Pickard, C. J.; Payne, M. C. Population Analysis of Plane-Wave Electronic Structure Calculations of Bulk Materials. *Phys. Rev. B: Condens. Matter Mater. Phys.* **1996**, *54*, 16317−16320.
(67) Dunnington, B. D.; Schmidt, J. R. Generalization of Natural Bond Orbital Analysis to Periodic Systems: Applications to Solids and Surfaces via Plane-Wave Density Functional Theory. *J. Chem. Theory Comput.* **2012**, *8*, 1902−1911.
(68) Pitzer, K. S. Relativistic Effects on Chemical Properties. *Acc. Chem. Res.* **1979**, *12*, 271−276.
(69) Ziegler, T.; Snijders, J. G.; Baerends, E. J. Relativistic Effects on Bonding. *J. Chem. Phys.* **1981**, *74*, 1271−1284.
(70) Kundu, S.; Bhattacharjee, S.; Lee, S.-C.; Jain, M. Population Analysis with Wannier Orbitals. *J. Chem. Phys.* **2021**, *154*, 104111.
(71) Lohr, L. L.; Pyykkö, P. Relativistically Parameterized Extended Hückel Theory. *Chem. Phys. Lett.* **1979**, *62*, 333−338.
(72) Pepperl, G.; Umlauf, E.; Meyer, A.; Keller, J. The Influence of Crystal Field Split Impurities (Tb) on the Superconducting Properties of LaAl2. *Solid State Commun.* **1974**, *14*, 161−165.
(73) Geballe, T. H.; Matthias, B. T.; Compton, V. B.; Corenzwit, E.; Hull, G. W.; Longinotti, L. D. Superconductivity in Binary Alloy Systems of the Rare Earths and of Thorium with Pt-Group Metals. *Phys. Rev.* **1965**, *137*, A119−A127.
(74) Chen, K. W.; Graf, D.; Besara, T.; Gallagher, A.; Kikugawa, N.; Balicas, L.; Siegrist, T.; Shekhter, A.; Baumbach, R. E. Temperature-Pressure Phase Diagram of Cubic Laves Phase Au2Pb. *Phys. Rev. B* **2016**, *93*, 045118.
(75) Zhang, J.; Jia, Y.; Wang, X.; Li, Z.; Duan, L.; Li, W.; Zhao, J.; Cao, L.; Dai, G.; Deng, Z.; et al. A New Quasi-One-Dimensional Compound Ba 3 TiTe 5 and Superconductivity Induced by Pressure. *NPG Asia Mater.* **2019**, *11*, 60.
(76) Yamaguchi, Y.; Waki, S.; Mitsugi, K. Superconductivity of YbSb2. *J. Phys. Soc. Jpn.* **1987**, *56*, 419−420.
(77) Yajima, T.; Takeiri, F.; Nozaki, Y.; Li, Z.; Tohyama, T.; Green, M. A.; Kobayashi, Y.; Kageyama, H. Superconductivity in the Hypervalent Compound Ba2Bi(Sb1−xBix)2 with a Square-Honeycomb Lattice. *J. Phys. Soc. Jpn.* **2014**, *83*, 073705.
(78) Havinga, E. E.; Damsma, H.; Van Maaren, M. H. Oscillatory Dependence of Superconductive Critical Temperature on Number of Valency Electrons in Cu3Au-Type Alloys. *J. Phys. Chem. Solids* **1970**, *31*, 2653−2662.
(79) Kinjo, T.; Kajino, S.; Nishio, T.; Kawashima, K.; Yanagi, Y.; Hase, I.; Yanagisawa, T.; Ishida, S.; Kito, H.; Takeshita, N.; et al. Superconductivity in LaBi3 with AuCu3-Type Structure. *Supercond. Sci. Technol.* **2016**, *29*, 03LT02.

Recommended by ACS

Pressure Dependence of Superconductivity in a Charge-Density-Wave Superconductor $Bi_2Rh_3Se_2$
Mitsuki Ikeda, Yoshihiro Kubozono, *et al.*
MAY 04, 2023
INORGANIC CHEMISTRY
READ

Non-Centrosymmetric Sr_2IrO_4 Obtained Under High Pressure
Haozhe Wang, Weiwei Xie, *et al.*
JANUARY 20, 2023
INORGANIC CHEMISTRY
READ

Superconductivity in Te-Deficient $ZrTe_2$
Lucas E. Correa, Antonio J. S. Machado, *et al.*
MARCH 08, 2023
THE JOURNAL OF PHYSICAL CHEMISTRY C
READ

Superconducting Behavior of $BaTi_2(Sb_{1-y}Bi_y)_2O$ under Pressure
Mitsuki Ikeda, Yoshihiro Kubozono, *et al.*
DECEMBER 08, 2022
INORGANIC CHEMISTRY
READ

Get More Suggestions >

MOST WIEDZY Downloaded from mostwiedzy.pl

https://doi.org/10.1021/acs.jpcc.3c02176
J. Phys. Chem. C 2023, 127, 14402−14414